An Experimental and Numerical Study of Novel Nano-grained $(\gamma + \alpha_2)$-TiAl/Al_2O_3 Cermets

B. Amirian[a], H.Y. Li[a], J.D. Hogan[a,*]

[a]*Department of Mechanical Engineering, The University of Alberta, Edmonton, AB T6G 2R3, Canada*

Abstract

In this paper, a microstructure-based finite element model for nano-grained $(\gamma+\alpha_2)$-TiAl/Al_2O_3 cermets is proposed based on a modified variational formulation of the Gurson model for an elastic-plastic porous material. In the modeling approach, the high volume fraction of alumina, variability in material characteristics, and microstructural features (e.g., inclusion size) are considered. Mechanical properties and microstructure inputs are derived from nanoindentation and microscopy analysis performed for this study, as well as using available information in the literature. Once developed, modeling results are validated against experimental quasi-static compressive stress-strain measurements using digital image correlation techniques. The validation is extended by comparing experimental observations and computational outputs of the ratio of the lateral to axial strain (as a measure of deformation), and reasonable agreement is found. Once the model is validated for an experimentally known condition, the effect of varying the mechanical properties (e.g., strain hardening parameters and elastic modulus) and microstructure variables (e.g., alumina volume fraction and porosity) on material responses are then explored. These results serve as a foundation for future microstructure optimization.

Keywords: Finite element models; Modified variational formulation; Cermet; Uniaxial compression test; Digital image correlation

1. Introduction

Structural ceramics have properties necessary to allow them to serve as structural components subjected to mechanical stress. Many of these ceramics also exhibit other attractive properties, such as resistance to deformation at high temperature [1], excellent chemical stability [2], high hardness [3], and high wear resistance [4]. Taken together, these properties make many structural ceramics

*Corresponding author
Email addresses: benhour@ualberta.ca (B. Amirian), haoyang@ualberta.ca (H.Y. Li), jdhogan@ualberta.ca (J.D. Hogan)

suitable for application in light-weight ballistic armor [5], and as medical applications and dental implants [6, 7]. In these and many other applications, the monolithic form of these ceramics are susceptiple to catastrophic brittle fracture. To remedy this, researchers have attempted to improve the ductility and fracture toughness of ceramics by combining the high toughness of metals with the high hardness, strength, and stiffness of the structural ceramics [8, 9, 10]. In the ceramic-metal materials, one can classify materials containing more than 50 vol.% metal as metal matrix composites (MMCs) [11, 12], and those containing more than 50 vol.% ceramic as cermets [13, 14]. In this paper, we investigate the elastic characteristics and strength of cermets.

Cermets typically have strengths that range between 2 and 7 times the strength of the metal matrix composites, and this allows them to be a potential candidate for aerospace and defense applications [14, 15, 16]. Compared with structural ceramics, cermets have higher fracture toughness and higher flexural strength [17]. To further the use of ceramic-metal materials in industrial applications, this paper focuses on understanding the linkages between mechanical responses (e.g., stress-strain behavior and deformation mechanisms), and microstructure characteristics (e.g., inclusion size and porosity). This is studied both experimentally and computationally for $(\gamma+\alpha_2)$-TiAl/Al_2O_3 cermets.

Achieving more favorable engineering properties in TiAl (e.g., high ductility and toughness) can be obtained by incorporating $(\gamma+\alpha_2)$ phase in the TiAl material [18]. The $(\gamma+\alpha_2)$-TiAl is believed to exhibit improved mechanical properties over its monolithic constituents as a result of greater volume fractions of lamellar grains, which are the result of the $\alpha \rightarrow \gamma$ phase transformation and eutectoid reactions [19]. Prior studies of $(\gamma+\alpha_2)$-TiAl family of materials include the processing and fabrication of dense alumina-TiAl-Ti_3Al [20], the oxidation behavior of in-situ TiAl/Al_2O_3 [21], and microstructure characteristics of synthesized TiAl/Al_2O_3 [22, 23, 24]. Altogether, these studies have advanced our understanding of the material science of these material systems. To date, no studies have focused on the mechanical behavior and numerical modeling of these materials, which is addressed in this paper.

There are numerous predictive models that are used to desribe the mechanical properties of cermets [25, 26, 27]. In earlier studies, the limiting state of plastic collapse was used to relate the hardness of cermet to its microstructure [28]. Later, Engqvist et al. [29] proposed empirical models for hardness of cemented carbide by studying the interactions between the binder and the carbide. Among other modeling approaches, microstructural models such as unit cell models [30] and dislocation based models [31] have generated interest in predicting the strength of cermets. For example, in a study by Legarth [32], the non-monotonical effect of a material length scale parameter on the failure strain of MMCs was adopted using a unit cell approach. In a separate study, Bao

et al. [33] carried out the combination of continuum plasticity theory with unit cell modeling to study the non-deforming particles in reinforcing ductile matrix materials. Other microstructure-independent approaches, such as the self-consistent models, were developed for composites, however, their usefulness are limited to materials with a low particle volume fraction [34]. In some commercial cermets, the particle volume fraction can reach up to 80% [35]. To date, the majority of the modeling efforts have concentrated on idealised microstructure configurations in conceptual ceramic-metal materials. Limited efforts have been made to bridge these models with experimental inputs [36, 37, 38]. In this present study, contributions are made towards these efforts by employing microstructural data as model inputs, and then using experimental data to validate the model.

Building on these previous works, the aim of this paper is to develop a three-dimensional face centered cubic (FCC) unit cell model of $(\gamma + \alpha_2)$-TiAl/Al_2O_3 commercial cermet. A modified variational formulation of the Gurson model (MVAR) for elasto-plastic porous materials is used for the host material that is based on the nonlinear homogenization approach. In order to derive the constitutive equations, the generalized midpoint rule is applied for integrating the stress-strain relations and solved the governing equations which are numerically implemented in a user-material-subroutine (UMAT) in finite element approach (FEA) using Abaqus. Once the model is implemented, scanning electron microscopy (SEM) images are used for characterization of porosity, alumina volume fraction, and void clusters as model inputs. Nanoindentation tests are used to provided inputs for stiffness for the matrix $(\gamma + \alpha_2)$-TiAl, and the reinforcement Al_2O_3 materials. Following this, quasi-static uniaxial compression tests are performed and coupled with digital image correlation techniques to determine the stress-strain responses of the material, as well as the corresponding ratio of axial and lateral strain during loading. These experimental inputs are then used to validate the unit cell model. Following implementation and validation, the influences of the variability of the stiffness and volume fraction of alumina nano-particles, along with void volume fraction (porosity) on the stress-strain behavior of cermet are discussed in detail. The totality of the results allow us to further improve the material strength and performance through material optimization.

2. Experimental procedures and results

2.1. Material composition and microstructure

The $(\gamma + \alpha_2)$-TiAl/Al_2O_3 cermet being investigated in this paper is fabricated through self-propagation high-temperature sintering, and is provided by Lumiant Corporation, British Columbia. Cermet tiles are cut into specimens with size of 2.3 mm (length) × 2.5 mm (width) × 2.7 mm (height)

for mechanical testings. Shown in Figure 1 is a backscattered electron (BSE) SEM image (Figure 1a) with energy dispersive X-ray spectroscopy (EDS) density maps of the elements: Al (Figure 1b), Ti (Figure 1c), and O (Figure 1d). Altogether, Figure 1 is used to reveal the spatial distribution of the phases within the material, with brighter colors in Figure 1b to Figure 1d corresponding to higher concentrations and darker colors corresponding to lower concentrations. This information is used for as modelling inputs.

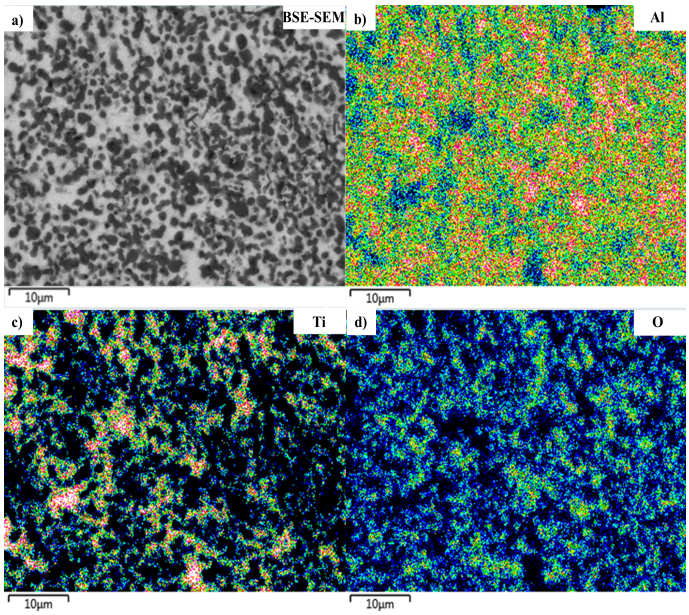

Figure 1: EDS concentration mapping on a 2000 times magnification SEM image showing distributions of selected element. Concentration of elements decrease based on the color sequence in the visible light spectrum. Brighter colors correspond to higher concentrations: a) FESEM image showing the phase distribution, where black regions correspond to the alumina phase and white regions correspond to the TiAl phase; b) Distribution and concentration of Al element in the FESEM image; c) Distribution and concentration of Ti element in the FESEM image; (d) Distribution and concentration of O element in the FESEM image.

In the Figure 1a, the lighter regions correspond to the TiAl phase because of the higher Z (atomic number) value; consequently, the darker regions are the Al_2O_3 phase. The darkest spots in the BSE figure correspond to the micro-pores present in the material, which have been confirmed with the field emission SEM (FESEM) images. It is observed that the pores tend to cluster around the boundary or within the alumina phase. To further analyze the features in the images, a MATLAB-based program was developed to quantify the areal fractions of the alumina and titanium aluminide phases, as well as the sizes of the alumina particles and pores. These methods are consistent with those developed in Hogan et al. [39]. To accomplish this, the SEM image was first converted to a binary image, and each pixel of the binary image was then discretized based on its greyscale from 0-255 (for uint8 type image). Pure white was assigned the number of 255, and pure black was assigned the number of 0. A threshold was carefully selected to isolate the black (or white) regions,

which corresponded to either alumina (inclusion) or titanium aluminide (matrix) phase. In this case, it was easier to isolate the white TiAl phase. As an outcome of this analysis, the porosity level is determined as 1.2 % to 3% at 2000 times magnification depending on a threshold setting. These values are within the range that is reported by the manufacture of 2 %. Using similar image processing techniques, the average pore size was $0.07 \pm 0.02\,\mu$m, as measured by the major axis. The individual alumina particles appear spherical in shape and in clusters in the material with sizes of 0.5 to $1.5\,\mu$m with an average of $1 \pm 0.3\,\mu$m, and clusters sizes of 3 to $9\,\mu$m. The area fraction of the alumina phase is estimated as 65 % $\pm$ 1 % using the same image processing techniques.

Next, the concentration of constitutive elements are investigated using energy dispersive X-ray microanalysis. Again, the regions in red in the figures correspond to higher concentrations of the element in the sub-figure, whereas blue and darker colors correspond to areas of lower concentrations of the elements. From Figure 1b, it is observed that Al is present everywhere in the material, with higher concentration in the alumina phase (darker phase in the SEM image). Comparing the Al (Figure 1b) with the Ti (Figure 1c) concentrations, we observe that regions of higher concentrations of Al correspond to regions of lower concentrations of Ti. Similarly, regions of higher concentrations of Al correspond to regions of higher concentrations of O, which are believed to be the Al_2O_3 phases with trace amounts of O with the Ti and Al. This is the α_2-TiAl phases (confirmed with X-ray diffraction (XRD) but not shown for brevity).

2.2. Experimental setup

The quasi-static uniaxial compression test was conducted on a standard MTS series 810 servo-hydraulic machine. Loading platens were made from hardened steel (M2 high speed steel) and were held in alignment by the machine grip. Ti-6Al-4V titanium alloy jacketed tungsten carbide (WC) platens were used between the specimen and the loading platens to provide stress re-distribution from the specimen to the loading platens, as well as to protect the machine load platens from indentation of the hard specimens. This is required by the ASTM C1424-15 [40]. As required, extreme pressure grease was applied on the WC platen surfaces to eliminate the frictional effect. The platens were then pre-loaded without specimen to create a thin, uniform layer of lubricant. The specimens were then carefully placed at the middle of the platens. Good alignment was ensured by carefully bringing the platens and specimen in touch. The experiment was performed under displacement control with a nominal strain rate of $1 \times 10^{-4}\,\mathrm{s}^{-1}$. The cross-head displacement was measured by a linear variable differential transformer displacement sensor with an accuracy of 0.001 mm. A 100 kN load cell with background noise corresponding to approximately ± 1 N was used to record

the force history during loading process. The acquisition rate of the MTS machine was set at 30 Hz. An AOS PROMON U750 high speed camera was used to provide visualization on macroscopic deformation features on the specimen surface. The specimen was positioned normally to the optical axis of the camera to eliminate out-of-plane displacement. This camera has a full resolution of 1280×1024 pixels and recorded at a frame rate of 100 frames per second. The engineering stresses were calculated by dividing the applied load by original specimen surface area, and the engineering strains were determined by employing DIC techniques, which is detailed in the next section. In total, five experiments are presented in this paper at the same loading condition to study variability and validate the model.

2.3. Digital image correlation technique

2.3.1. Methodology

Digital image correlation was used to obtain the global strain field from the specimen surface during compression testing. The Correlated Solutions VIC2D 6 software [41] was used to produce the full-field strain measurements. In DIC analysis, a small subset of an image is tracked as the specimen translates and deforms. In each image, the subset in the deformed images are shifted to match the pattern in the reference image; the "match" is performed as the total difference in gray level at each point. In order to obtain the displacement information by tracking the deformation or displacement of subsets, a correlation peak is determined as the gray level for each subset [42]. The position of the peaks provides the local displacement and the height of the peaks gives the degree of correlation. During the analysis, the zero-normalized squared sum of difference (ZNSSD) method was chosen to perform the correlation. This method is known to be highly robust, which will not be affected by the offset and scale in lighting [43]. Gaussian low pass filter was selected to eliminate the high frequency signals and pre-smooth both reference and deformed images. This pre-smoothing will increase the accuracy of the measurement because it filters out the bias signals. The "Optimized 8-tap" interpolation scheme in the software was selected, which incorporated the highest order of spline scheme. In post processing, the rigid body motion was removed to compensate any possible vibration on the camera or the machine, which was deemed minimal in this experiment.

2.3.2. Setup

To obtain accurate and robust analysis, sample preparation is always the first and one of the most essential steps. Considering the size of our specimen ($2.3 \times 2.5 \times 2.7$ mm), applying a relatively good speckle pattern is crucial in performing these measurements, where a non-repetitive, isotropic,

and high contrast speckle pattern is desired. Conventional speckle pattern kits, or other methods, such as regular spray paint, are not applicable on specimens of our size. In the experiment, an ultra-fine point airbrush with 0.12 mm needle and nozzle was used to spray specialize airbrush paint with particle size down to 0.1 μm onto the specimen surface. A thin, white base coating was applied on the as-received shiny specimen surface to have a uniform background. Black speckles were then sprayed on the base coat with a continuously sweeping motion.

Lighting and contrasting is another issue associated with good analysis. In these experiments, an ultra-bright LED light equipped with fiber optical light guide with a 7.6 mm diameter liquid light guide was used to provide high intensity uniform lighting environment over the specimen surface. A highly contrasted and overexposed surface condition was obtained. According to Jerabek et al. [44], a fine speckle pattern and appropriate light intensity gives a better result when it is under the condition of overexposure. With good specimen preparation and lighting environment, the PROMON U750 camera was used to capture the deformation process of the specimen. With the first image as the reference (undeformed) image and appropriate area of interest (AOI), the "suggested subset" function in the VIC2D package is used to obtain the proposed subset size with minimum estimated error. This could be used as an alternative way to examine the goodness of speckle pattern. It was observed that a consistent subset size was obtained on all specimens used in this paper, where all subset sizes were in the range of 23×23 to 30×30 pixels. To perform the analysis, the correlation step size was altered in each selected AOI from 2 to 7 based on the noise level to determine the optimal results. Several AOIs were tested in each experiment to examine the repeatability of the results, including failure strain, strain rate, and slope change between axial and lateral strains. Finally, the smoothest strain field with least aliasing was picked and imported into MATLAB for further analysis with the stress data. Details on sensitivity analysis and filtering are beyond the scope of this study.

2.4. Experimental results

2.4.1. The stress-strain response of $(\gamma + \alpha_2)$-$TiAl/Al_2O_3$

Shown in Figure 2 is the engineering stress-strain plot of the material from the quasi-static uniaxial compression tests. The naming of the specimens follows the DIC speckle pattern sequences (i.e., sp1, sp2, etc). In total, five stress-strain curves are plotted. Specimens sp1, sp4, and sp5 are tests that successfully showing the repeatability of the experiments. Some outliers, such as sp2 and sp3 in the figure, correspond to potential microstructural variabilities and surface deformation features during loading (sp3 had a visible fracture form on its surface at the corresponding dip in

the stress). These are included to demonstrate the variability in the results.

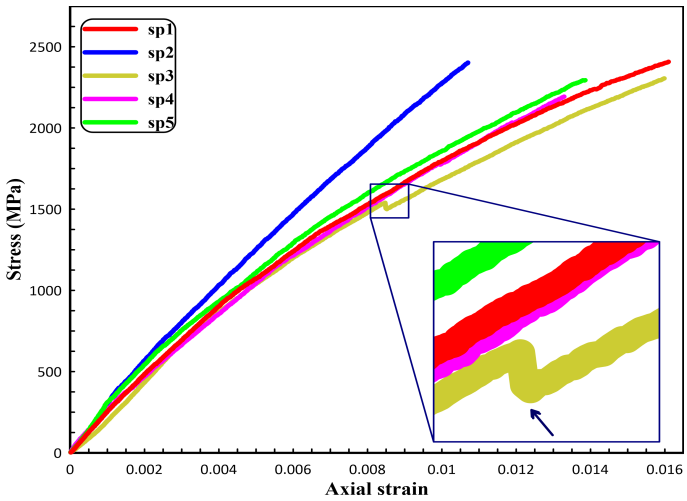

Figure 2: Variations of the experimental engineering stress with the DIC engineering strain

From the figure, the failure strain of the materials is between 1.1% and 1.7%, with an average of 1.4% $\pm$ 0.2%. The compressive strength is between 2200 and 2600 MPa, with an average of 2400 $\pm$ 120 MPa. Strain hardening effects are observed on all curves, which indicates ductility in the material when compared to, for example, alumina. Similar shaped curves for cermets have been reported by others in the literature [45, 46]. The slope of the initial part of the stress-strain curve, taken as the Young's modulus of the material, is between 240 and 310 GPa, with an average of 274 $\pm$ 26 GPa.

2.4.2. The transverse and axial strain ratio during loading

Next, we examine the ratio of transverse (ϵ_{yy}) to longitudinal (ϵ_{xx}) strain in Figure 3. Color schemes follow those from Figure 2. Again, three curves are presented for repeatability and two outliers are shown for potential microstructural variability. In Figure 3, the initial lateral to longitudinal strain ratio across all five samples is 0.227 with a standard deviation of 0.001. The ratio of lateral to longitudinal strain at the initial constant portion is identified as the Poisson's ratio of the intact material, which corresponds to the first order approximation for small values of length change. The value reported here is reasonable as the Poisson's ratio for alumina is 0.220 reported by Coorstek [47], and for gamma phase titanium aluminide is 0.230-0.240 [48].

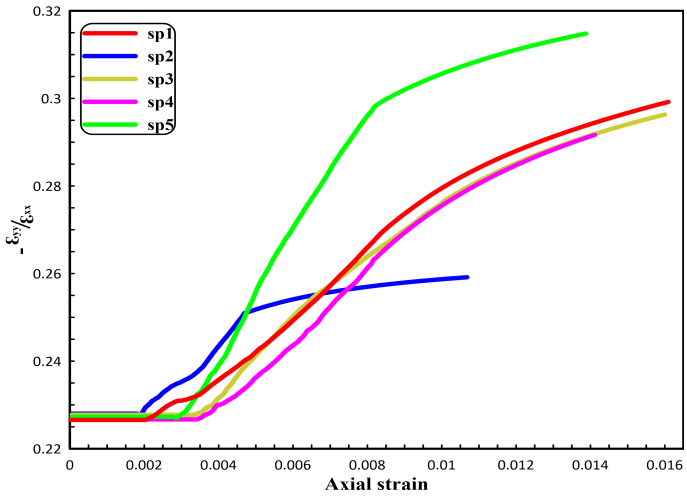

Figure 3: Variation of the lateral and longitudinal strain ratio with the DIC strain

After the initial part of the curve, the ratio of lateral to longitudinal strain could be a representation of the deformation mechanisms that manifest in the material during loading. In Figure 3, all curves start near a constant value of 0.227 and remains flat until 0.2 % to 0.4 % strain, after which time the curves increase at variable rates until maximum values of 0.250 to 0.320 (average of 0.290 $\pm$ 0.020). The rise in the curves is a consequence of damage accumulation, and this appears to be increasing at a greater rate in the lateral direction (perpendicular to compression) than the axial direction (parallel to compression). Here, material failure is likely through a combination of plastic deformation and fracture. In tests sp1, sp3, and sp4, the ratio rises to approximately 0.300 before failure. Specimen sp2 shows a significantly lower final ratio than other tests at much lower failure strain. In addition, specimen sp5 has a much greater failure strain and higher final strain ratio. The reason for this is unknown, but is also likely due to the microstructural variability. Interestingly, no discernible features other than a minor transition in slopes is observed for sp3, where cracking occurred during compression testing. Altogether, these results provide insights into material deformation, and will serve as data sets for validation our modeling efforts described next.

3. Numerical modeling of $(\gamma + \alpha_2)$-TiAl/Al_2O_3 cermets

3.1. Microstructure representation

In this paper, the microstructure is modeled as a two phase material: (i) the elastic-plastic and isotropic matrix $(\gamma + \alpha_2)$-TiAl phase, and (ii) the inclusion Al_2O_3 phase. Porosity is also generated by means of a Mathematica code. The microstructure representation is considered by ellipsoidal voids with both equal or unequal semi-axes a_1, a_2 and a_3, and this is shown schematically in Figure

4. Here, a three dimensional unit cell with spherical isotropic elastic particles of alumina in a voided elastoplastic matrix is modeled. In our modeling approaches, the FCC crystal structure arrangement is considered in order to allow us to achieve representative volumetric densities of the secondary alumina phase ($\sim$ 65 %).

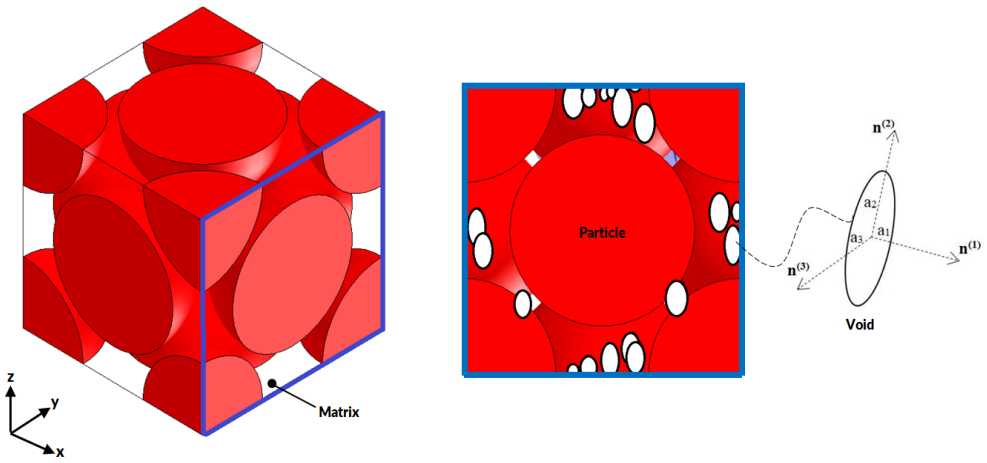

Figure 4: Schematic representation of microstructures presenting the local orientation axes of an ellipsoidal void with semi-axes a_1, a_2 and a_3.

In these simulations, the set of internal variables for describing the general state of microstructure are: accumulated plastic strain in the undamaged matrix ε_p^M, the volume fraction of the voids f, the local fraction of volume occupied by voids, two aspect ratios characterizing the ellipsoidal shape of the voids (w_1 and w_2) and their distribution functions, and the orientation of the principal axes of the voids (n_i with $i = 1, 2, 3$).

3.2. Constitutive equations

The deformation behavior of $(\gamma + \alpha_2)$-TiAl/Al_2O_3 material is distinguished by separating it into recoverable and nonrecoverable parts based on the additive decomposition of strain rates. The rate of deformation tensor D, at every material point of the homogenized porous material is written as

$$D = D^{el} + D^{pl}, \tag{1}$$

where D^{el} and D^{pl} are the elastic and plastic parts, respectively. As a consequence of the compressibility of the material behavior due to presence of voids, the plastic strain rate tensor is only hydrostatic. In this case, linear elasticity is assumed for simplicity as

$$\sigma = D^{el} : \varepsilon^{el}, \tag{2}$$

which is the relation between the Cauchy stress σ, and elastic strain tensors ε^{el} through the fourth-order elasticity tensor D^{el}. A hypoelastic form is assumed for the elastic deformation tensor as

$$D^{el} = M^e : \mathring{\sigma}, \tag{3}$$

where M^e is the effective elastic compliance tensor and $\mathring{\sigma}$ is the corotational rate of the Cauchy stress given by

$$\mathring{\sigma} = \dot{\sigma} - \omega \cdot \sigma + \sigma \cdot \omega, \tag{4}$$

where ω is the spin of voids relative to a fixed frame, i.e., $\dot{n}^i = \omega \cdot n^i, i = 1, 2, 3$. The effective compliance tensor is written as [49]

$$M^e = M + \frac{f}{1-f} Q^{-1}, \tag{5}$$

In Eq. (5), M is the elastic compliance tensor of the matrix material which is the inverse of the elastic modulus tensor E

$$\begin{aligned} E &= 2\mu K + 3\kappa \mathbb{J}, & (6)\\ \mathbb{J} &= \frac{1}{3}\delta\delta, & (7)\\ K &= \mathbb{I} - \mathbb{J}, & (8)\\ Q &= E : (\mathbb{I} - \mathbb{S}), & (9)\\ \mathbb{I}_{ijkl} &= \frac{\delta_{ik}\delta_{jl} + \delta_{il}\delta_{jk}}{2}, & (10) \end{aligned}$$

where μ and κ denote the elastic shear and bulk moduli of the matrix, δ and $\mathbb{I}$ are the symmetric second- and fourth-order identity tensors, f is the porosity, $\mathbb{S}$ is the fourth-order Eshelby tensor, and Q is the microstructural fourth-order tensor which is proportional to the shear modulus, Poisson's ratio, aspect ratio of the voids, and also the orientation of the ellipsoidal voids [50].

The derivation of the constitutive relations is the variational procedure that is used to estimate the effective properties of the nonlinear porous material in terms of an appropriate linear comparison composite. The effective yield function can be written in the form [51]

$$\Phi(\sigma, s) = \frac{1}{1-f} \sigma : m : \sigma - \sigma_y^2(\bar{\varepsilon}^p), \tag{11}$$

where s is the set of internal variables; σ_y is the yield strength in tension of matrix material and is taken to be a function of the equivalent plastic strain $\bar{\varepsilon}^p$ in the matrix material. Here, m is normalized effective viscous compliance tensor and is defined as

$$m = \frac{3}{2}K + \frac{3}{1-f}\mu Q^{-1}|_{\nu=0.5}, \tag{12}$$

where the limit for Poisson's ratio is due to assumption of plastic incompressibility. It is emphasized that the plastic behavior described by the macroscopic potential is fully compressible. If we limit our model to spherical voids, whose shape remain unchanged during deformation, the MVAR model reduces to the Gurson isotropic model

$$\Phi(\sigma, \bar{\varepsilon}^p, f) = \left(1 + \frac{2}{3}f\right)\left(\frac{\sigma_e}{1-f}\right)^2 + \frac{9}{4}f\left(\frac{p}{1-f}\right)^2 - \sigma_y^2(\bar{\varepsilon}^p) = 0, \tag{13}$$

where $\sigma_e = (\frac{3}{2}\sigma^d\colon \sigma^d)^{0.5}$ is the equivalent von Mises stress, $\sigma^d = \sigma - p\delta$ is the deviatoric part of the stress, and $p = \frac{1}{3}\sigma\colon I$ is the hydrostatic stress. It is assumed that only the plastic deformation of the matrix leads to change in microstructure because the voids do not carry load and the elastic strains are smaller than the plastic counterpart.

An effect of the mean normal stress on the plastic flow always exists when there is a non-vanishing void volume fraction. By implementing the normality hypothesis of plasticity, the plastic rate of deformation tensor is obtained by

$$D^{pl} = \dot{\lambda}\boldsymbol{N}, \tag{14}$$

$$\boldsymbol{N} = \frac{\partial\Phi}{\partial\sigma} = \frac{2}{1-f}m\colon\sigma, \tag{15}$$

where $\dot{\lambda} \geq 0$ is the plastic multiplier which can be obtained by consistency condition, and $\boldsymbol{N}$ is the direction of the plastic strain increment. With consideration of the equal relation between the macroscopic plastic work and microscopic work

$$\sigma\colon D^{pl} \equiv \dot{\lambda}\sigma\boldsymbol{N} = (1-f)\sigma_y\dot{\bar{\varepsilon}}^p, \tag{16}$$

the evolution of equivalent plastic strain is then obtained by

$$\dot{\bar{\varepsilon}}^p = \frac{\dot{\lambda}\sigma\colon\boldsymbol{N}}{(1-f)\sigma_y}, \tag{17}$$

For the damage evolution, the matrix material is assumed to be plastically incompressible (von Mises type) and the elastic volumetric strains are negligible. The evolution equation for porosity from the continuity equation is given by

$$\dot{f} = (1 - f) D^p_{kk}, \tag{18}$$

where D^p_{kk} is the volumetric part of the plastic rate of deformation tensor and can be integrated to calculate the current f. The strain hardening response of the material matrix, following the J_2 flow rule, is described by the yield stress σ_y as a function of the accumulated equivalent plastic strain $\bar{\varepsilon}^p$ [49]

$$\sigma_y(\varepsilon^p_M) = \sigma_0 \left(1 + \frac{\varepsilon^p_M}{\varepsilon_0}\right)^n, \varepsilon_0 = \frac{\sigma_0}{E}. \tag{19}$$

In this expression, σ_0 and ε_0 are the initial yield stress and strain, respectively, and n is the strain hardening exponent.

In the MVAR model, a critical void volume fraction is used as a fracture criteria such that the damage evolution accelerates as the damage parameter reaches to a critical value. This characterizes the rapidly growing void volume fraction in the void coalescence phase. In Eq. (18), one can use a damage rate coefficient K_D, which is defined as

$$K_D = \begin{cases} 1 & D \leq D_c, \\ \frac{f_m - f_c}{f_f - f_c} & D_c < D \leq 1, \end{cases} \tag{20}$$

where D_c is the damage critical value, f_f is the volume fraction at failure ($f = f_f$), f_c is the critical value of void volume fraction at coalescence under uniaxial tension, and $f_m = {}^1/_{q_1}$ with q_1 as a constant parameter introduced by Tvergaard [52]. This function was introduced by Tvergaard and Needleman [53] in order to account for the loss of load carrying capacity after void coalescence.

In order to implement the local integration scheme, two methods have been commonly used: Runge-Kutta and the fully implicit method. In both schemes, the integrated variables are the elastic strain tensor ε_e, the accumulated plastic strain $\bar{\varepsilon}^p$, and the void volume fraction (porosity) f. In this paper, we have used the fully implicit method with Newton-Raphson (N-R) scheme, which is the optimal choice for solving the constitutive equation because of the quadratic rates of convergence. This integration algorithm is first-order accurate, unconditionally stable, and easy for using the consistent tangent operators in the general N-R procedure. For implementing the fully

implicit method, the generalized midpoint rule was used because of its efficiency. The integration algorithm of the constitutive equations for MVAR model is listed in Box-I.

Box-I. Local incremental integration algorithm for modified variational formulation model

1. The elastoplastic constitutive initial value problem

$$\dot{\varepsilon^e}(t) = \dot{\varepsilon}(t) - (1-f)\dot{\varepsilon^p}(t)\boldsymbol{N}, \tag{21}$$

$$\dot{f}(t) = (1-f)^2 tr(\boldsymbol{N})\ \dot{\varepsilon^p}(t). \tag{22}$$

2. The incremental form of constitutive equation

$$\varepsilon^e_{n+1} = \varepsilon^e_n + \Delta\varepsilon - (1-f)\Delta\varepsilon^p \boldsymbol{N}, \tag{23}$$

$$f_{n+1} = f_n + (1-f)^2 tr\boldsymbol{N}\ \Delta\varepsilon^p, \tag{24}$$

$$\Phi(\sigma_{n+1}, A_{n+1}) = 0; \quad \sigma_{n+1} = \bar{\rho}\ \frac{\partial\psi}{\partial\varepsilon^e}\bigg|_{n+1} \quad \text{and} \quad A_{n+1} = \bar{\rho}\ \frac{\partial\psi}{\partial f}\bigg|_{n+1}. \tag{25}$$

3. The general viscoplastic constitutive equations

$$\varepsilon^e_{n+1} - \Delta\varepsilon + \Delta t g(\sigma_{n+1}, A_{n+1}) = 0, \tag{26}$$

$$f_{n+1} - f_n - \Delta t J(\sigma_{n+1}, A_{n+1}) = 0. \tag{27}$$

with consideration of

$$g\left(\sigma(t), A(t)\right) = \dot{\lambda}(\sigma(t), A(t))\ N(\sigma(t), A(t)), \tag{28}$$

$$J(\sigma(t), A(t)) = \dot{\lambda}(\sigma(t), A(t))\ H(\sigma(t), A(t)). \tag{29}$$

where in our case we have

$$g(\sigma(t), A(t)) = (1-f)\Delta\varepsilon^p\boldsymbol{N},\ J(\sigma(t), A(t)) = (1-f)^2 tr(\boldsymbol{N})\Delta\varepsilon^p. \tag{30}$$

4. The linearized system of time-discrete equations

$$d\varepsilon^e + \Delta t \frac{\partial g}{\partial \sigma} : d\sigma + \Delta t \frac{\partial g}{\partial A} * dA = d\Delta\varepsilon \tag{31}$$

$$df - \Delta t \frac{\partial J}{\partial \sigma} * d\sigma + \Delta t \frac{\partial J}{\partial A} * dA = 0, \tag{32}$$

where * is the appropriate product and

$$g_{n+\theta} = g((1-\theta)\sigma_{n+1} + \theta\sigma_n, (1-\theta)A_n + \theta A_{n+1}), \tag{33}$$

$$J_{n+\theta} = g((1-\theta)\sigma_{n+1} + \theta\sigma_n, (1-\theta)H_n + \theta H_{n+1}). \tag{34}$$

5. The complete set of constitutive relations

$$\begin{pmatrix} \frac{\partial R^e}{\partial \Delta\varepsilon^e} & \frac{\partial R^e}{\partial \Delta\varepsilon^p} & \frac{\partial R^e}{\partial f} \\ \frac{\partial R^p}{\partial \Delta\varepsilon^e} & \frac{\partial R^p}{\partial \Delta\varepsilon^p} & \frac{\partial R^p}{\partial f} \\ \frac{\partial R^f}{\partial \Delta\varepsilon^e} & \frac{\partial R^f}{\partial \Delta\varepsilon^p} & \frac{\partial R^f}{\partial f} \end{pmatrix} \begin{pmatrix} \Delta\varepsilon^e + \Delta\varepsilon^p \\ \Delta f - \Delta t \dot{f} \\ \Phi(\sigma_{n+1}, A_{n+1}) \end{pmatrix} = \begin{pmatrix} \Delta\varepsilon \\ 0 \\ 0 \end{pmatrix}, \tag{35}$$

where

$$R^e = \Delta\varepsilon^e - \Delta\varepsilon + (1-f)\Delta\varepsilon^p \ \boldsymbol{N}, \tag{36}$$

$$R^p = \Delta\varepsilon^p - \Phi(\sigma, s)\Delta t \tag{37}$$

$$R^f = \Delta f - (1-f)^2 \Delta\varepsilon^p \ tr(\boldsymbol{N}), \tag{38}$$

6. The Jacobian matrix components

$$\begin{aligned} &\frac{\partial R^e}{\partial \Delta\varepsilon^e} = \mathbb{I} + (1-f)\Delta\varepsilon^p \frac{\partial \boldsymbol{N}}{\partial \sigma} : D^e\theta; \quad \frac{\partial R^e}{\partial \Delta\varepsilon^p} = (1-f)\boldsymbol{N}; \\ &\frac{\partial R^e}{\partial \Delta f} = -\Delta\varepsilon^p \boldsymbol{N} + (1-f)\Delta\varepsilon^p \frac{\partial \boldsymbol{N}}{\partial f}; \quad \frac{\partial R^p}{\partial \Delta\varepsilon^p} = (1-f)\boldsymbol{N}; \quad \frac{\partial R^p}{\partial \Delta\varepsilon^e} = \boldsymbol{N} : D^e\theta; \\ &\frac{\partial R^p}{\partial \Delta\varepsilon^p} = -\frac{\partial \sigma_y}{\partial \varepsilon^p}; \quad \frac{\partial R^p}{\partial \Delta f} = \frac{\partial \sigma_e}{\partial f}; \quad \frac{\partial R^f}{\partial \Delta\varepsilon^e} = -(1-f)^2 \Delta\varepsilon^p \theta\mathbb{I}; \quad \frac{\partial R^f}{\partial \Delta\varepsilon^p} = -(1-f)^2\mathbb{I} : \boldsymbol{N}; \\ &\frac{\partial R^f}{\partial \Delta f} = 1 + \Delta\varepsilon^p \theta(1-f)\mathbb{I} : \left(2\boldsymbol{N} - (1-f)\frac{\partial \boldsymbol{N}}{\partial f}\right). \end{aligned} \tag{39}$$

4. Model validation and application

4.1. Model validation

Until now, a three-dimensional FCC unit cell model of the $(\gamma + \alpha_2)$-TiAl/Al_2O_3 commercial cermet has been presented based on a modified variational formulation of the Gurson model. In this section, some experiments and microscopy analysis are used as inputs into the model, and then the model is validated against our compression experiments. The mechanical properties of the matrix, reinforcements, and the damage parameter values are given in Table 1. The elastic modulus of the two phases in the material, E_M and E_P, are determined by ultra nanoindentation using diamond Berkovich indentor, performed by Anton Paar. A matrix of 30×30 indents are performed on an area of $290 \times 290\,\mu$m. The values for ν_M, ν_P, σ_y^M, and f_0 are obtained from the literature. The baseline for the alumina volume fraction is 65 %. The ratio of the size length of the unit cell to diameter of the reinforcements is 1.477, and the pore size is 0.03 of the particle size.

Table 1: Material properties and the related damage parameters for each component

Parameters	Notation	Value	Reference
Young's modulus (Matrix)	E_M	$178 \pm 31\ GPa$	Nanoindentation test
Young's modulus (Particle)	E_P	$278 \pm 41\ GPa$	Nanoindentation test
Poisson's ratio (Matrix)	ν_M	0.23	[54]
Poisson's ratio (Particle)	ν_P	0.22	[47]
Yield stress (Matrix)	σ_y^M	$0.45\ GPa$	[54]
Initial porosity (Matrix)	f_0	0.01	[38]

In these simulations, the uniaxial compression stress is applied in the x direction with displacement control type loading. In the absent of voids, the matrix is assumed to have an initial yield strain of $\varepsilon_0 = 0.001$ [38]. The commercial Abaqus FEA is used for performing the calculations and a 10-node quadratic tetrahedron element (C3D10 in the Abaqus FEA notation) is employed for meshing the unit cell. The Dirichlet boundary condition is implemented for this simulation in order to compare with uniaxial compression experiments. Shown in Figure 5 is the engineering stress-strain curve obtained numerically, and compared with experimental data previously shown in Figure 2. In the curve, we vary the strain hardening modulus in the matrix material between 1 (b) to 2 GPa (a), because the strain hardening components are material parameters which are the most unknown in the model. From the figure, we observe that strain hardening components of $k = 1.5$ GPa and $n = 0.05$ (c) fit the data reasonably well, and are in acceptable ranges [55, 56]. We use these parameters in all subsequent modeling.

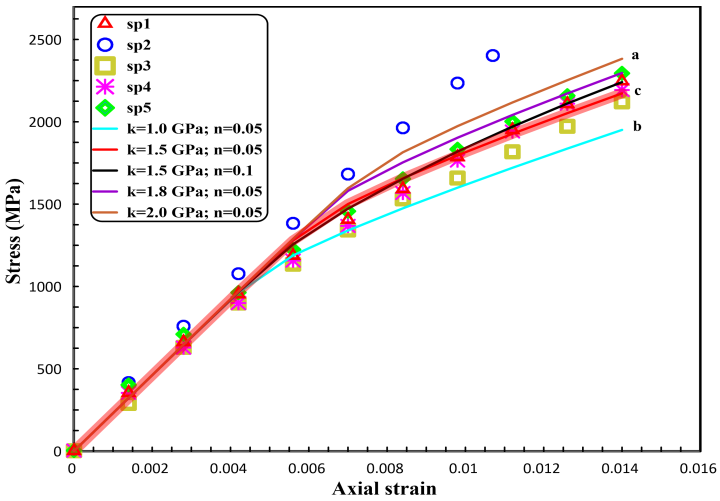

Figure 5: The engineering stress-strain behavior of ceramic-metal composite for various strain hardening parameters

Next, we examine the ability of the model to capture the experimental results in terms of stress-strain response. In order to study the experimental variability, 15 different realizations of the model were simulated based on varying matrix and particle stiffness. In these simulations, each alumina particle was assigned a different stiffness, and the matrix stiffness was left to vary, both assume a normal distribution about an average (from Table 1) with a 20% standard deviation. The summary of these simulations is shown in Figure 6 as the shaded regions, with realizations for the upper and lower bounds indicated in the legend. The realization that best fit the experimental data ($E_M = 178\,\text{GPa}$ and $E_P = 278\,\text{GPa}$) is indicated as a dashed-dot red line. Overall, the model reasonably captures the experimental stress-strain response considering how few parameters were fit to the experimental data.

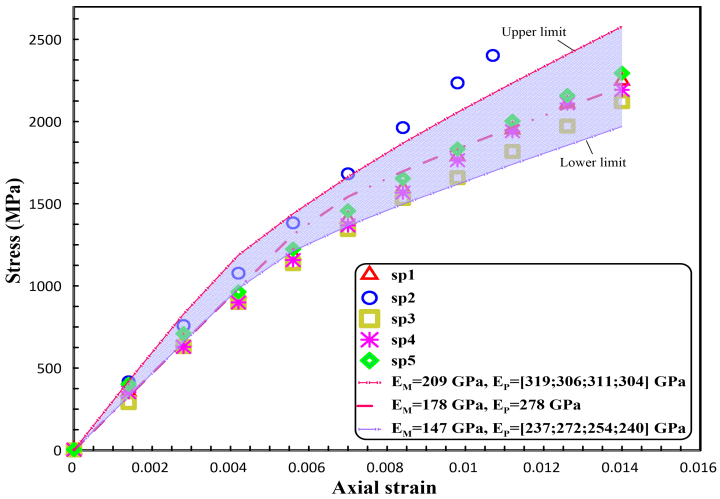

Figure 6: Variation of engineering stress versus engineering strain for both modeling results and experimental data

Next, the ability of the model to predict deformation observed in the experiment is investigated by plotting outputs of the lateral (ϵ_{yy}) over the axial (ϵ_{xx}) strain in Figure 7. As before, matrix and alumina particles stiffness were varied to probe variability in the model and experimental outputs. From Figure 7, we observe that the initial ratio of the lateral to axial strain computed numerically is 0.220 ± 0.002. This is slightly smaller than the experimental values (0.227 ± 0.001), but within reasonable agreement. The model seems to predict the onset of the transition to higher ratios at around 0.2 % to 0.4 % strain. The predicted peak value of the lateral to axial strain ratio is between 0.299 and 0.329, which is slightly greater than the experimental values, but still within reasonable magnitudes. The reasons for this are explained in the "Discussion" section. Altogether, these results indicate that the model framework with real-world inputs provide reasonable agreement with the experimentally-determined values of stress-strain responses and strain ratios.

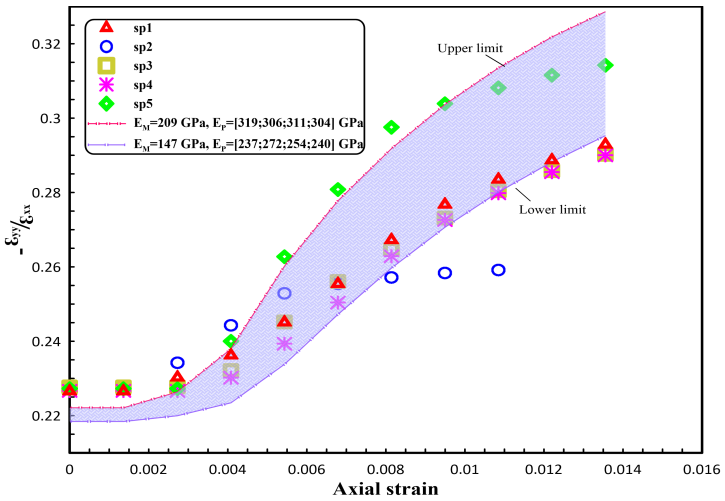

Figure 7: Variation of strain ratio during loading with axial strain

4.2. The effect of alumina volume fraction, porosity, and unit cell size

After showing a good correlation between the proposed model and experimental trends, we now explore the effects of varying the concentrations of the alumina phase and porosity in order to study the implications for future materials design. In these simulations, we take the baseline parameters included in Table 1, and we change the volume fraction of the alumina and pores. This is meant to simulate realistic changes that can be made to the microstructure through processing. First, we begin by investigating the effect of varying the volume fraction of the alumina particles on the engineering stress-strain behavior and ratio of lateral to axial strain (Figure 8). In this case, the particle sizes remained constant and different reinforcement volume fraction was obtained by changing the size of the unit cell. The baseline was considered for concentration of particles with an average of 65 % ±

7 %, which is believed to be an appropriate range to vary the alumina concentrations.

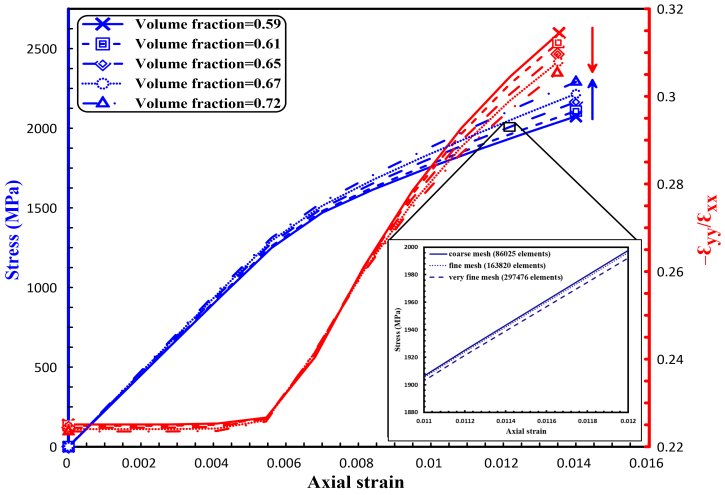

Figure 8: The effect of particle volume fraction on engineering stress-strain response and deformation profile of cermet during loading with consideration of various FE meshes (Arrows indicate increasing alumina volume fraction)

From Figure 8, the results show that increasing the alumina volume fraction from 65 % to 72 % (direction of marked arrow) can increase the peak stress by around 126 MPa ($\sim$ 6% of the current strength). Conversely, the peak strength decreases by 90 MPa when the volume fraction is decreased from 65 % to 59 %, which represents 4 % of the current strength. In addition, increasing the alumina particles volume fraction from 65 % to 72 % can lead to decreasing the maximum strain ratio by 0.004. Moreover, the onset of the transition to plastic region and higher strain ratios is predicted at around 0.4 % to 0.6 % strain. Lastly, the effect of different meshes on the results (very fine, fine, and coarse mesh) are plotted. The number of elements in each mesh is shown in the insert in Figure 8. The inset shows quite small differences in the material response for different number of elements, which shows mesh-insensitivity. Next, the effect of varying the void volume fraction and unit cell size ratio (S_{UC}), the ratio of the size length of the unit cell to diameter of the alumina particles, on the engineering stress-strain behavior and ratio of lateral to axial strain is investigated in Figure 9. The results were obtained assuming equiaxed pore morphology (voids with equal semi-axis), and uniformly random distribution at a constant alumina particle volume fraction (65 %). In addition, the baseline was considered for porosity values with an average of 1.5 % $\pm$ 0.7 %, which is believed to be a reasonable amount one could vary the porosity in this material. As can be observed in Figure 9, the peak stress value decreases with increasing void volume fraction (direction of marked arrow) from lowest ($f = 0.001$) to highest ($f = 0.03$) porosity values by 105 MPa ($\sim$ 5% of the current strength). Conversely, the strain ratio increases by 0.002 with increasing the void volume fraction from $f = 0.001$ to $f = 0.03$. With an increase in the unit cell size ratio, lower stress values were also

observed. Similar behavior was predicted for mechanical properties of carbon nanotube polymer composites [57]. Considering the highest value of porosity ($f = 0.03$), the strength is decreased by 152 MPa, by varying the unit cell size ratio from $S_{UC} = 1.447$ to $S_{UC} = 1.526$, which shows a 7 % reduction in the current strength. For lower porosity values ($f = 0.001$), the strength difference between values would be 168 MPa, 3 % change across the range of unit cell size ratios. Conversely, the strain ratio increases with increasing unit cell size ratio for $f = 0.03$ by 3 %. For all cases, mesh insensitivity is observed (not shown for brevity). Implications of these results are discussed in the following section.

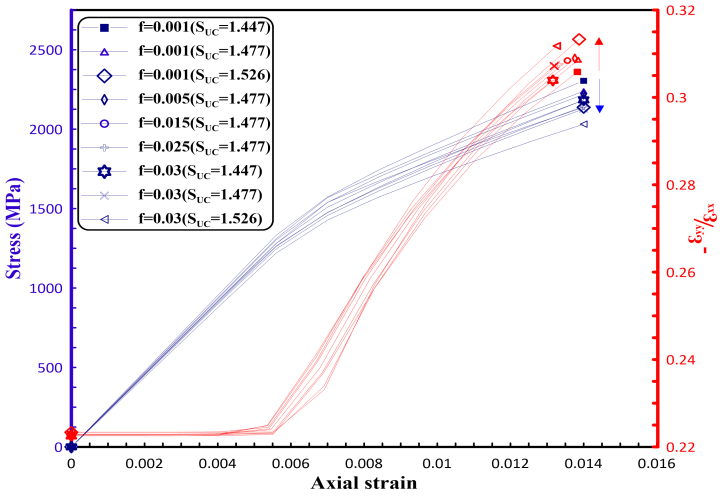

Figure 9: Predicted compressive engineering stress-strain curves and lateral to longitudinal ratio for the ceramic-metal composite with varying porosity and size of the unit cell (Arrows indicate increasing void volume fraction)

5. Discussions

In this study, a general modification of the Gurson-based models was proposed in order to investigate the micromechanical behavior of nano-grained ($\gamma + \alpha_2$)-TiAl/Al_2O_3 commercial cermets. Here, the previous works [58, 59, 60] on ductile nanoporous MMCs have been expanded to investigate the mechanical characteristics and the deformation profile of commercial cermets [61, 62] by incorporating a nonlinear homogenization variational structure for composites [63]. For the first time, a commercial cermet, rather than an idealised one [37], with high particles volume fraction (~ 65 %) has been studied both numerically and experimentally. Material characterization was done to generate microstructural inputs into the model, including measurements of alumina size (average of $1 \pm 0.3\,\mu$m), alumina volume fraction (65 % $\pm$ 1 %), porosity size (0.05 to 0.09 μm), and void volume fraction (1.2 % to 3 %). An FCC unit cell structure was considered as the microstructure of this novel oxide cermet to provide the highest possible reinforcement volume fraction. Once inputs

were made, the model was validated against experiments through comparison of the compressive stress-strain response and the ratio of lateral to axial strain. Experimental data was obtained from quasi-static uniaxial compression tests, coupled to novel DIC techniques. In the literature, limited measurements exist for the stress-strain response of cermets [46, 64, 65], likely due to the only recent advancements in the DIC technology. The stress-strain measurements on our cermet revealed that strength of the material was between 2200 and 2600 MPa, with an average of 2400 $\pm$ 120 MPa, the stiffness was between 240 and 310 GPa, with an average of 274 $\pm$ 26 GPa, and the failure strains were between 1.1% and 1.7%, with an average of 1.4% $\pm$ 0.2%. These values were much higher than the counterparts in MMCs [66] and idealised cermets [37], indicating the unique properties of this novel $(\gamma + \alpha_2)$-TiAl/Al_2O_3 cermet.

A comparison of the experimental and numerical results showed that the experimental values were in reasonable agreement with the numerical predictions of the stress-strain and ratio of strains responses (Figure 5 and 6). The numerical values for strength of the material was between 1970 and 2580 MPa, and the stiffness was between 220 and 260 GPa. Experimentally, minor differences may be attributed to residual stress in the material set as a consequence of different thermal contraction between the constituent phases [67], reinforcements fracture during manufacturing process or mechanical loading [68], and particle shape and clustering that contributes to damage accumulation, cracks nucleation sites, and degradation of the mechanical properties of the cermet [69]. Numerically, the uniform and homogeneous distribution of alumina assumed in the model likely results in higher stress-strain values and ratio of strains, when compared to experimental results. There may also be some degree of porosity in the actual material that is not captured in the model, which can occur either by the fracture of the inclusions or by decohesion of the particle-matrix interfaces [70], that accumulates during loading and acts to reduce the strain ratio. Moreover, the model simulates mostly uniform void growth and coalescence throughout the body, whereas the failure in the experiment is likely due to the growth and coalescence of a few voids/cracks [67]. Furthermore, there was a gradual transition from low to high strain ratio, both numerically and experimentally, which may attribute to different behavior of particle clustering as a single hard large particle or independent reinforcement [71] (Figure 7). Altogether, insights gained here for comparing the experiments and models can provide guidance for future work in directions motivated by discrepancies between the simulations and the test data.

Once the model was validated, the effect of changing the alumina volume fraction, porosity and unit cell size was explored. This exercise can provide valuable information for optimization the material mcirostructure for the mechanical response (e.g., strength, stiffness, Poisson's ratio

evolution). It was found that increasing the alumina particles volume fraction from 65% to 72% result in increasing the material strength by 6 %. Physically, this increase in alumina volume fraction would lead to larger interfacial area between matrix and particles, which can result in more effective load-bearing capacity and increase the strength [67]. For porosity, it was observed that reducing the porosity from its current level of 1.5 % to 0.1 % results in an increase in strength of 2.5 %. While possibly challenging to increase the alumina volume fraction and reduce the porosity to these levels, this information provides guidance to material manufactures with response to where efforts should be concentrated to improve the mechanical responses of this novel cermet material. For instance, reducing the presence of porosity sites such as fine oxide particles arising from manufacturing process can remove the barriers for dislocation motion in the matrix and increase the stiffness of the overall material [72].

6. Concluding remarks

In the present study, a modified variational formulation of the Gurson model was employed for predicting the quasi-static behavior of a $(\gamma + \alpha_2)$-TiAl/Al_2O_3 cermet. This is the first time this material has been studied extensively both numerically and experimentally. BSE-SEM and EDS analysis were used for determining the microstructure parameters as model inputs. Quasi-static uniaxial compression tests, coupled with DIC technique, were performed to investigate the mechanical response and corresponding evolution of the deformation profile during loading. Following implementation, the experimental inputs were used to validate the unit cell model and reasonable agreement was found. The strain hardening components, which were the most unknown material parameters, were obtained by matching the modeling results with experimental trends. The strength of 2209 $\pm$ 239 MPa, stiffness of 240 $\pm$ 20 GPa, and strain hardening modulus of 1.5 $\pm$ 0.5 GPa were predicted from the presented model, which were in good agreement with experimental data. Once validated, the effects and implications of different parameters such as particle volume fraction, porosity, unit cell size ratio, and the variability of the inclusion stiffness were presented and discussed. Altogether, it is speculated that the proposed model together with appropriate measurements can be accounted for representing the unique mechanical responses of other commercial cermets as well.

Acknowledgements

This research was sponsored by the Natural Sciences and Engineering Research Council of Canada with support from PRE Labs Inc. and Lumiant Corporation. We thank Calvin Lo and Bernie Faulker

for aiding in the completing the experiments.

References

[1] S. M. Wiederhorn, L.-S. H. Lum, Structural behavior of ceramics, Tech. rep. (2016).

[2] J. Yeomans, T. Page, The chemical stability of ceramic cutting tool materials exposed to liquid metals, Wear 131 (1) (1989) 163–175.

[3] M. Anglada, Assessment of mechanical properties of ceramic materials, in: Advances in Ceramic Biomaterials, Elsevier, 2017, pp. 83–109.

[4] M.-S. Suh, Y.-H. Chae, S.-S. Kim, Friction and wear behavior of structural ceramics sliding against zirconia, Wear 264 (9-10) (2008) 800–806.

[5] E. Medvedovski, Ballistic performance of armour ceramics: Influence of design and structure. Part I, Ceramics International 36 (7) (2010) 2103–2115.

[6] J. Chevalier, L. Gremillard, Ceramics for medical applications: A picture for the next 20 years, Journal of the European Ceramic Society 29 (7) (2009) 1245–1255.

[7] L. L. Hench, Bioceramics, a clinical success, American Ceramic Society Bulletin 77 (7) (1998) 67–74.

[8] J. Silvestre, N. Silvestre, J. De Brito, An overview on the improvement of mechanical properties of ceramics nanocomposites, Journal of Nanomaterials 2015 (2015) 3.

[9] M. Estili, A. Kawasaki, H. Sakamoto, Y. Mekuchi, M. Kuno, T. Tsukada, The homogeneous dispersion of surfactantless, slightly disordered, crystalline, multiwalled carbon nanotubes in α-alumina ceramics for structural reinforcement, Acta Materialia 56 (15) (2008) 4070–4079.

[10] D. Djenkal, D. Goeuriot, F. Thevenot, Sic-reinforcement of an Al2O3–γAlON composite, Journal of the European Ceramic Society 20 (14-15) (2000) 2585–2590.

[11] C. G. Mangin, J. A. Isaacs, J. P. Clark, MMCs for automotive engine applications, JoM 48 (2) (1996) 49–51.

[12] D. Zhang, G. Zhang, Z. LI, The current state and trend of metal matrix composites, Materials China 29 (4) (2010) 1–7.

[13] D. Liu, W. Tuan, Microstructure and thermal conduction properties of Al2O3-Ag composites, Acta Materialia 44 (2) (1996) 813–818.

[14] B. Compton, F. Zok, Impact resistance of TiC-based cermets, International Journal of Impact Engineering 62 (2013) 75–87.

[15] M. Karamis, F. Nair, A. Tasdemirci, Analyses of metallurgical behavior of Al–SiCp composites after ballistic impacts, Composite Structures 64 (2) (2004) 219–226.

[16] H. Chang, J. Binner, R. Higginson, P. Myers, P. Webb, G. King, High strain rate characteristics of 3-3 metal–ceramic interpenetrating composites, Materials Science and Engineering: A 528 (6) (2011) 2239–2245.

[17] V. Verma, B. M. Kumar, Processing of TiCN–WC–Ni/Co cermets via conventional and spark plasma sintering technique, Transactions of the Indian Institute of Metals 70 (3) (2017) 843–853.

[18] M. Yamaguchi, H. Inui, K. Ito, High-temperature structural intermetallics, Acta Materialia 48 (1) (2000) 307–322.

[19] Y.-W. Kim, D. M. Dimiduk, Progress in the understanding of gamma titanium aluminides, JoM 43 (8) (1991) 40–47.

[20] C. M. Ward-Close, R. Minor, P. J. Doorbar, Intermetallic-matrix composites—a review, Intermetallics 4 (3) (1996) 217–229.

[21] T.-t. Ai, F. Wang, X.-m. Feng, Oxidation behavior of in-situ Al2O3/TiAl composites at 900° c in static air, International Journal of Minerals, Metallurgy and Materials 16 (3) (2009) 339–344.

[22] L. Y. Xiang, F. Wang, J. F. Zhu, X. F. Wang, Microstructure and mechanical properties of Al2O3/TiAl in situ composites doped with Fe2O3, in: Materials Science Forum, Vol. 675, Trans Tech Publ, 2011, pp. 597–600.

[23] W.-H. Wei, Z.-N. Shao, J. Shen, X.-M. Duan, Microstructure and mechanical properties of in situ formed TiC-reinforced Ti–6Al–4V matrix composites, Materials Science and Technology 34 (2) (2018) 191–198.

[24] L. Xiang, F. Wang, J. Zhu, X. Wang, Mechanical properties and microstructure of Al2O3/TiAl in situ composites doped with Cr2O3, Materials Science and Engineering: A 528 (9) (2011) 3337–3341.

[25] Z. Hashin, S. Shtrikman, A variational approach to the theory of the elastic behaviour of multiphase materials, Journal of the Mechanics and Physics of Solids 11 (2) (1963) 127–140.

[26] M. Starink, S. Syngellakis, Shear lag models for discontinuous composites: fibre end stresses and weak interface layers, Materials Science and Engineering: A 270 (2) (1999) 270–277.

[27] P. A. Cundall, O. D. Strack, A discrete numerical model for granular assemblies, Geotechnique 29 (1) (1979) 47–65.

[28] J. Pelletier, P. Sallamand, B. Criqui, Microstructure and mechanical properties of some metal matrix composites produced on different materials by laser cladding, Lasers in Engineering 3 (1994) 15–27.

[29] H. Engqvist, S. Jacobson, N. Axén, A model for the hardness of cemented carbides, Wear 252 (5-6) (2002) 384–393.

[30] N. Shi, M. Bourke, J. Roberts, J. Allison, Phase-stress partition during uniaxial tensile loading of a TiC-particulate-reinforced Al composite, Metallurgical and Materials Transactions A 28 (12) (1997) 2741–2753.

[31] T. Gustafson, P. Panda, G. Song, R. Raj, Influence of microstructural scale on plastic flow behavior of metal matrix composites, Acta Materialia 45 (4) (1997) 1633–1643.

[32] B. N. Legarth, Plasticity dependent damage evolution in composites with strain-gradient effects, International Journal of Solids and Structures 63 (2015) 1–10.

[33] G. Bao, J. Hutchinson, R. McMeeking, Particle reinforcement of ductile matrices against plastic flow and creep, Acta Metallurgica et Materialia 39 (8) (1991) 1871–1882.

[34] R. Hill, A self-consistent mechanics of composite materials, Journal of the Mechanics and Physics of Solids 13 (4) (1965) 213–222.

[35] C.-h. Liu, S. R. Nagel, D. Schecter, S. Coppersmith, S. Majumdar, O. Narayan, T. Witten, Force fluctuations in bead packs, Science 269 (5223) (1995) 513–515.

[36] T. Christman, A. Needleman, S. Suresh, An experimental and numerical study of deformation in metal-ceramic composites, Acta Metallurgica 37 (11) (1989) 3029–3050.

[37] E. Bele, V. S. Deshpande, The compressive response of idealized cermetlike materials, Journal of Applied Mechanics 82 (4) (2015) 041009.

[38] E. Bele, A. Goel, E. Pickering, G. Borstnar, O. Katsamenis, F. Pierron, K. Danas, V. Deshpande, Deformation mechanisms of idealised cermets under multi-axial loading, Journal of the Mechanics and Physics of Solids 102 (2017) 80–100.

[39] J. D. Hogan, L. Farbaniec, T. Sano, M. Shaeffer, K. Ramesh, The effects of defects on the uniaxial compressive strength and failure of an advanced ceramic, Acta Materialia 102 (2016) 263–272.

[40] ASTM C1425-15. Standard test method for monotonic compressive strength of advanced ceramics at ambient temperature, West Conshohocken (PA).

[41] Vic-2D , Correlated Solutions Inc, Irmo, South Carolina.
URL http://correlatedsolutions.com/vic-2d/

[42] B. Pan, K. Qian, H. Xie, A. Asundi, Two-dimensional digital image correlation for in-plane displacement and strain measurement: a review, Measurement Science and Technology 20 (6) (2009) 062001.

[43] S.-W. Khoo, S. Karuppanan, C.-S. Tan, A review of surface deformation and strain measurement using two-dimensional digital image correlation, Metrology and Measurement Systems 23 (3) (2016) 461–480.

[44] M. Jerabek, Z. Major, R. Lang, Strain determination of polymeric materials using digital image correlation, Polymer Testing 29 (3) (2010) 407–416.

[45] M. J. Kerper, L. E. Mong, M. B. Stiefel, S. F. Holley, Evaluation of tensile, compressive, torsional, transverse, and impact tests and correlation of results for brittle cermets, Journal of Research of the National Bureau of Standards 61 (3) (1958) 149.

[46] A. R. Kamali, S. Hadavi, J. Baboee, H. Razavizadeh, Production of TiAl (Ti3Al)/Al2O3 nanocomposite, in: Journal of Nano Research, Vol. 3, Trans Tech Publ, 2008, pp. 7–14.

[47] CoorsTek Inc., Advanced alumina brochure, http://www.coorstek.com/media/1715/advanced-alumina-brochure.pdf (2016).

[48] Y. He, R. Schwarz, A. Migliori, S. Whang, Elastic constants of single crystal γ–TiAl, Journal of Materials Research 10 (5) (1995) 1187–1195.

[49] K. Danas, N. Aravas, Numerical modeling of elasto-plastic porous materials with void shape effects at finite deformations, Composites Part B: Engineering 43 (6) (2012) 2544–2559.

[50] N. Aravas, P. P. Castañeda, Numerical methods for porous metals with deformation-induced anisotropy, Computer Methods in Applied Mechanics and Engineering 193 (36-38) (2004) 3767–3805.

[51] M. Kailasam, P. P. Castaneda, A general constitutive theory for linear and nonlinear particulate media with microstructure evolution, Journal of the Mechanics and Physics of Solids 46 (3) (1998) 427–465.

[52] V. Tvergaard, Material failure by void coalescence in localized shear bands, International Journal of Solids and Structures 18 (8) (1982) 659–672.

[53] V. Tvergaard, A. Needleman, Analysis of the cup-cone fracture in a round tensile bar, Acta Metallurgica 32 (1) (1984) 157–169.

[54] F. Appel, J. D. H. Paul, M. Oehring, Gamma titanium aluminide alloys: science and technology, John Wiley & Sons, 2011.

[55] C. de Formanoir, A. Brulard, S. Vivès, G. Martin, F. Prima, S. Michotte, E. Rivière, A. Dolimont, S. Godet, A strategy to improve the work-hardening behavior of Ti–6Al–4V parts produced by additive manufacturing, Materials Research Letters 5 (3) (2017) 201–208.

[56] H. Yildiz, O. Sayman, M. Aktaş, Effects of hardening parameter and strain hardening exponent on residual stress and plastic zone growth in aluminum metal–matrix composites under out-of-plane loading, Journal of Reinforced Plastics and Composites 23 (18) (2004) 2065–2080.

[57] M. Malagù, M. Goudarzi, A. Lyulin, E. Benvenuti, A. Simone, Diameter-dependent elastic properties of carbon nanotube-polymer composites: Emergence of size effects from atomistic-scale simulations, Composites Part B: Engineering 131 (2017) 260–281.

[58] V. Monchiet, D. Kondo, Combined voids size and shape effects on the macroscopic criterion of ductile nanoporous materials, International Journal of Plasticity 43 (2013) 20–41.

[59] T. Goudarzi, R. Avazmohammadi, R. Naghdabadi, Surface energy effects on the yield strength of nanoporous materials containing nanoscale cylindrical voids, Mechanics of Materials 42 (9) (2010) 852–862.

[60] W. Zhang, T. Wang, X. Chen, Effect of surface/interface stress on the plastic deformation of nanoporous materials and nanocomposites, International Journal of Plasticity 26 (7) (2010) 957–975.

[61] I. C. Getting, G. Chen, J. A. Brown, The strength and rheology of commercial tungsten carbide cermets used in high-pressure apparatus, in: Experimental Techniques in Mineral and Rock Physics, Springer, 1993, pp. 545–577.

[62] E. Pickering, E. Bele, V. Deshpande, Multi-axial response of idealized cermets, Acta Materialia 116 (2016) 281–289.

[63] P. P. Castañeda, The effective mechanical properties of nonlinear isotropic composites, Journal of the Mechanics and Physics of Solids 39 (1) (1991) 45–71.

[64] T. D. Huy, H. Fujiwara, R. Yoshida, T. B. Do, H. Miyamoto, Microstructure and mechanical properties of TiAl3/Al2O3 in situ composite by combustion process, Materials Transactions 55 (7) (2014) 1091–1093.

[65] S. Scudino, G. Liu, K. Prashanth, B. Bartusch, K. Surreddi, B. Murty, J. Eckert, Mechanical properties of Al-based metal matrix composites reinforced with Zr-based glassy particles produced by powder metallurgy, Acta Materialia 57 (6) (2009) 2029–2039.

[66] C. Feng, L. Froyen, In-situ P/M Al/(ZrB2+ Al2O3) MMCs: processing, microstructure and mechanical characterization, Acta Materialia 47 (18) (1999) 4571–4583.

[67] N. Chawla, Y.-L. Shen, Mechanical behavior of particle reinforced metal matrix composites, Advanced Engineering Materials 3 (6) (2001) 357–370.

[68] Y.-L. Shen, M. Finot, A. Needleman, S. Suresh, Effective plastic response of two-phase composites, Acta Metallurgica et Materialia 43 (4) (1995) 1701–1722.

[69] L. Chingshen, F. Ellyin, Fatigue damage and its localization in particulate metal matrix composites, Materials Science and Engineering: A 214 (1-2) (1996) 115–121.

[70] M. Taya, H. Lilholt, in advances in compiosite materials and structures, ASME (1986) 21–27.

[71] B. Park, A. Crosky, A. Hellier, Material characterisation and mechanical properties of Al2O3-Al metal matrix composites, Journal of Materials Science 36 (10) (2001) 2417–2426.

[72] K.-T. Park, E. J. Lavernia, F. A. Mohamed, High temperature creep of silicon carbide particulate reinforced aluminum, Acta Metallurgica et Materialia 38 (11) (1990) 2149–2159.